Bulletin of the Seismological Society of America, Vol. 87, No. 1, pp. 97–113, February 1997

An Empirical Study of Earthquake Source Spectra for California Earthquakes

by Gail M. Atkinson and Walt Silva

Abstract We generalize source, path, and site effects for California earthquakes as functions of magnitude and distance, based on regression analysis of 1000 Fourier acceleration spectra from 43 California earthquakes in the moment magnitude range from 4.4 to 7.4, recorded at rupture distances from 1 to 200 km. Empirically derived source spectra for California earthquakes are generally inconsistent with the spectral shape implied by a Brune ("omega-squared") point-source model. This is manifested by magnitude- and frequency-dependence of the Brune model parameters. For example, the Brune stress parameter that best matches the data at high frequencies decreases from a value of about 120 bars at **M**5.5 to a value near 50 bars at **M**7.5. At frequencies below 1 Hz, though, source spectra have much lower spectral amplitudes than predicted by the Brune point-source model for these values of stress; this discrepancy grows with increasing magnitude. Finite-fault simulations indicate that this is a consequence of the breakdown of the validity of the point-source approximation for large ruptures. A stochastic finite-fault model, in which the fault is discretized as a number of subfaults, each of which is represented by a Brune omega-squared point source, correctly matches the observed spectral shapes and amplitudes.

The spectral decay parameter kappa, representing average near-surface attenuation of high-frequency motion at rock sites, increases with increasing magnitude, from values near 0.035 sec at **M**5.5 to 0.050 sec at **M**7.5. Magnitude dependence of kappa may be interpreted as evidence of nonlinearity for typical California sites subjected to strong ground motion.

Comparisons of our empirical source spectra for California to corresponding spectra for eastern North America suggest that the spectral amplitudes are similar in the two regions for low-frequency motions ($f < 2$ Hz for **M**5.5, $f < 0.5$ Hz for **M**7.5), for equivalent crustal conditions. The eastern events appear to have enhanced high-frequency near-source amplitudes relative to the California events; this is particularly pronounced for large-magnitude earthquakes.

Introduction

In the past decade, studies of California earthquakes have become increasingly focused on the details of source, path, and site processes. Thanks to improved modeling techniques, coupled with an impressive increase in strong-motion and broadband databases, detailed modeling of the nature and distribution of slip during major events has become almost routine (e.g., Hartzell and Heaton, 1986; Hartzell and Iida, 1990; Wald *et al.*, 1991; Steidl *et al.*, 1991; Wald and Heaton, 1994). Modeling has advanced our understanding of many aspects of the faulting process and how they relate to the generation of strong ground motion.

Unfortunately, this enthusiasm for understanding the details of ground-motion generation has not been matched by attempts to generalize the underlying source and propagation processes. Broadbrush empirical studies are important for two reasons:

1. generalizations are most useful for predicting future ground motions, since details are generally not repeatable from one event to the next; and
2. by characterizing average or typical behavior, we can better understand how individual events fit into the overall framework.

One of the most widely applied and successful tools for characterizing the significant and stable features of ground motion has been the stochastic model (Hanks and McGuire, 1981; Boore, 1983; Boore *et al.*, 1992; Silva, 1992; Schneider *et al.*, 1993; EPRI, 1993; Atkinson and Boore, 1995;

Silva and Darragh, 1995). Ground motion is modeled by bandlimited Gaussian noise, whose underlying spectrum is given by a seismological model of the overall source and path processes. The model predicts observed ground motions with a degree of accuracy that rivals that of more detailed source modeling and wave propagation methods (Schneider *et al.,* 1993; Atkinson and Somerville, 1994). The stochastic model has provided a simple and effective framework for guiding and interpreting empirical ground-motion relations. Such models are critical in extending predictions to magnitude–distance ranges that are not well constrained by data.

The accuracy and reliability of simple models for the prediction of ground motions depends entirely on our ability to characterize the basic input processes: we must be able to quantify source, path, and site effects as functions of magnitude and distance. California earthquakes have typically been described using a simple Brune (1970, 1971) point-source model, from which the horizontal-component Fourier spectrum of acceleration near the earthquake source can be described as a function of the seismic moment (M_0, in dyne-cm), a stress parameter ($\Delta\sigma$, in bars), and a site or regional value of near-surface attenuation, kappa (κ_0; Anderson and Hough, 1984):

$$A(f) = CV(f)\, M_0\, (2\pi f)^2 \exp(-\pi f \kappa_0)/[1 + (f/f_o)^2] \quad (1)$$

with $C = \mathcal{R}_P\, FH/(4\pi\mathcal{S}\beta^3\, R)$, and $f_o = 4.9 \times 10^6\, \beta(\Delta\sigma/M_0)^{1/3}$, where $\mathcal{R}_P$ = average radiation pattern (0.55 for shear waves), F = free surface amplification (2.0), H = partition onto two horizontal components ($1/\sqrt{2}$), $\mathcal{S}$ = crustal density (2.7 g/cm^3), and β = shear-wave velocity in the source region (3.2 km/sec). $V(f)$, as tabulated in the Appendix, provides the amplification of shear-wave amplitudes through a typical California crustal velocity gradient (Boore, 1986), illustrated in Figure 1. The factor $V(f)$ is generally neglected in modeling eastern North American (ENA) ground motions (e.g., Atkinson, 1993; Atkinson and Boore, 1995; Silva and Darragh, 1995); $V(f)$ is close to unity for ENA hard-rock sites due to the much steeper velocity gradient of the crust (Fig. 1). In equation (1), note that the Brune spectrum features a single-corner frequency, f_o, which is determined by the stress parameter and the seismic moment.

Analysis of California source parameters typically report Brune stress parameters in the range of 30 to 100 bars (e.g., Kanamori and Anderson, 1975; Hough and Dreger, 1995). A Brune model with $\Delta\sigma$ in the range from 50 to 100 bars, in conjunction with the stochastic approach, has had remarkable success in describing a number of observed ground-motion characteristics (Hanks and McGuire, 1981; Boore, 1983; Boore *et al.,* 1992; Silva and Darragh, 1995).

Departures from the simple Brune model may be expected for large events, for which the single-corner-frequency representation may be unrealistic. The factors that would give rise to more than one corner frequency in the spectrum include a rectangular (as opposed to circular) rupture (Savage, 1972), partial stress drop (Brune, 1970), and fault "roughness" (Gusev, 1983), interpreted as either barriers (Papageorgiou and Aki, 1983) or asperities (Hartzell and Brune, 1979). These factors may explain why the source spectra of some California earthquakes appear to "sag" at intermediate frequencies ($\lesssim$1 Hz), relative to the predictions of the Brune point-source model (Schneider *et al.,* 1993; Silva and Darragh, 1995). This sag at intermediate frequencies is also an inferred characteristic of the source spectra of large earthquakes in eastern North America (Boatwright and Choy, 1992; Atkinson, 1993).

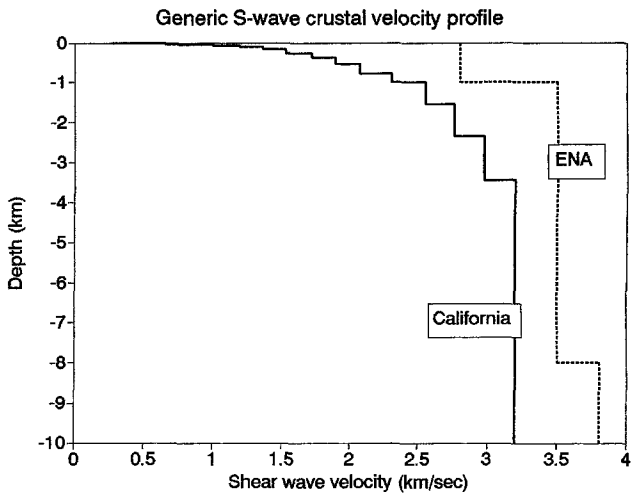

Figure 1. Comparison of average shear-wave velocity profile for California (Boore, 1986; personal comm., 1988) (solid line) with eastern rock profile, based on well log data at Moodus, Connecticut, and seismic reflection data (dotted line). Modified from Silva and Darragh (1995).

In this study, we use regression techniques to analyze a database of over 1000 reprocessed Fourier acceleration spectra from 43 California earthquakes, in the moment magnitude (**M**) range from 4.4 to 7.4, at rupture distances from 1 to 200 km. We determine the source spectra, the average regional attenuation, and the average response of "soil" sites relative to "rock" sites. The source spectra are compared to the predictions of the Brune point-source model and to predictions of a finite-fault model. The finite-fault model is an extension of the stochastic point-source model, in which the fault plane is discretized into a number of subfaults, each of which is represented as a Brune point source. Fourier spectra for the finite-fault model are characterized by averaging the predicted ground motions over a number of random slip distributions and station azimuths. We also compare the California source spectra to corresponding source spectra for ENA.

Regression Analysis of California Fourier Spectra Database

Database

The database is comprised of Fourier spectra computed from acceleration time histories from 43 California earth-

quakes of moment magnitude (**M**) 4.4 to 7.4, listed in the Appendix table. The distribution of the database in magnitude and distance is shown in Figure 2. Only free-field or equivalent records (e.g., basement of building less than two stories in height) are considered. Events are analyzed only if recorded by at least three such stations. Each recording site is classified according to Geomatrix site categories A through E (EPRI, 1993) as follows:

A = rock ($\beta > 600$ m/sec) or <5 m soil over rock,
B = stiff shallow (<20 m) soil over rock,
C = deep (>20 m) firm soil in narrow canyon or valley,
D = deep (>20 m) firm soil in broad valley, and
E = deep soft ($\beta < 180$ m/sec) soil.

When detailed site information was unavailable, the classification was generally made based on geologic maps (therefore, there is some uncertainty in the classifications). Sites classified as E (soft soil) were not used in the analysis (there were too few E sites to reliably determine the soil response coefficients). Initial regression analyses indicated that categories A and B could be combined (as r = soft rock, 431 records) and that C and D could be combined (as s = soil, 724 records). This increased the number of records for each category, providing more robust regression results. Note that the definition of "soft rock" is rather liberal, but this is probably a reasonable representation of typical California rock conditions.

Available "Volume 1" (i.e., uncorrected) records were reprocessed to extend the useable bandwidths where possible and to provide a uniform processing standard. Processing consisted of interpolation to 600 samples/sec, low-pass filtering at 30 to 50 Hz, decimation to 200 samples/sec, and finally, the computation of Fourier amplitude spectra for the *S*-wave train, including all of the strongest shaking. Final filter corner frequencies (high- and low-pass) were selected based on visual examination of the Fourier amplitude spectra. Processed displacement time histories were examined to check long-period noise levels (base-line drifts); the records were then refiltered if contamination was apparent. The final low-pass filters are fourth-order causal Butterworth, while the high-pass filters are fifth-order causal Butterworth.

Fourier spectra were examined for the frequency range 0.2 to 12 Hz (where possible), for each of two horizontal components, and the log amplitudes of the acceleration spectrum were tabulated at frequencies having a spacing of 0.15 log frequency units (since we typically model log amplitude versus log frequency). Log amplitudes were averaged within each frequency "bin" centered about the tabulated frequency; thus, amplitudes are smoothed over all frequencies within a factor of 1.19 ($10^{0.15/2}$) of the tabulated frequency.

The distance measure is the closest distance from the recording station to the rupture surface. For small earthquakes (**M** < 6.5) or those for which the fault plane is not defined, the hypocentral distance is used.

Figure 3 provides an example of the Fourier data for

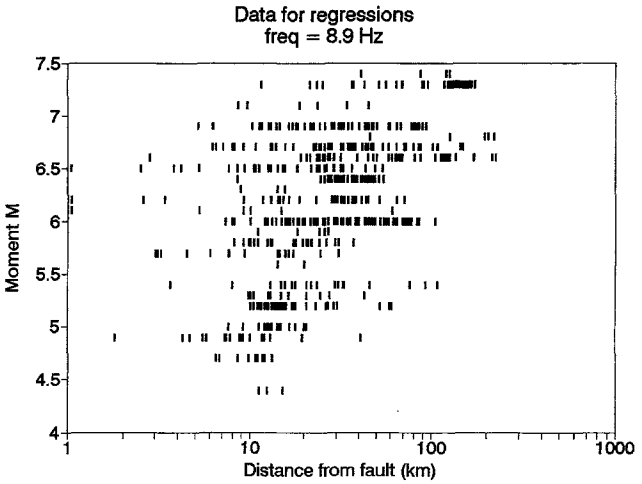

Figure 2. Distribution of spectral data for regression analysis in moment magnitude and distance.

two earthquakes, the 1984 Morgan Hill and 1989 Loma Prieta events. The figure compares the rock data at rupture distances near 20 km to the spectra predicted by a Brune point-source model with a 50-bar stress drop at this distance, assuming $\kappa_0 = 0.055$; the kappa value was chosen to match the high-frequency shape for these two events. The figure supports the suggestion that there may be a sag at intermediate frequencies, relative to the predictions of the Brune point-source model.

Regression Method

The Fourier acceleration database is regressed, frequency by frequency, to an equation of the following form:

$$\log A_{ij}(f) = \log A_{io}(f) - b \log R_{ij} - c(f) R_{ij} + \log S_j(f), \quad (2)$$

where $A_{ij}(f)$ is the observed spectral amplitude of earthquake i at station j, for the frequency f; $A_{io}(f)$ is the source amplitude of earthquake i; R is distance; b is the geometric spreading coefficient; $c(f)$ is the coefficient of anelastic attenuation (inversely proportional to quality factor, Q); and $S_j(f)$ is the site-response term for the soil category corresponding to station j, under the constraint that $\log S(f) = 0$ for rock sites. This is a standard equation form for empirical regressions of ground-motion data. The source terms and attenuation coefficients of such analyses can be related to the parameters of a number of potential physical models, such as that provided by equation (1).

The regression uses the iterative grid-search technique described by Atkinson and Mereu (1992), which is based on an L1 norm (e.g., minimizes the sum of the absolute value of the errors). The regression scheme allows the geometric spreading coefficient b to take on different (possibly frequency-dependent) values in each of three distance ranges:

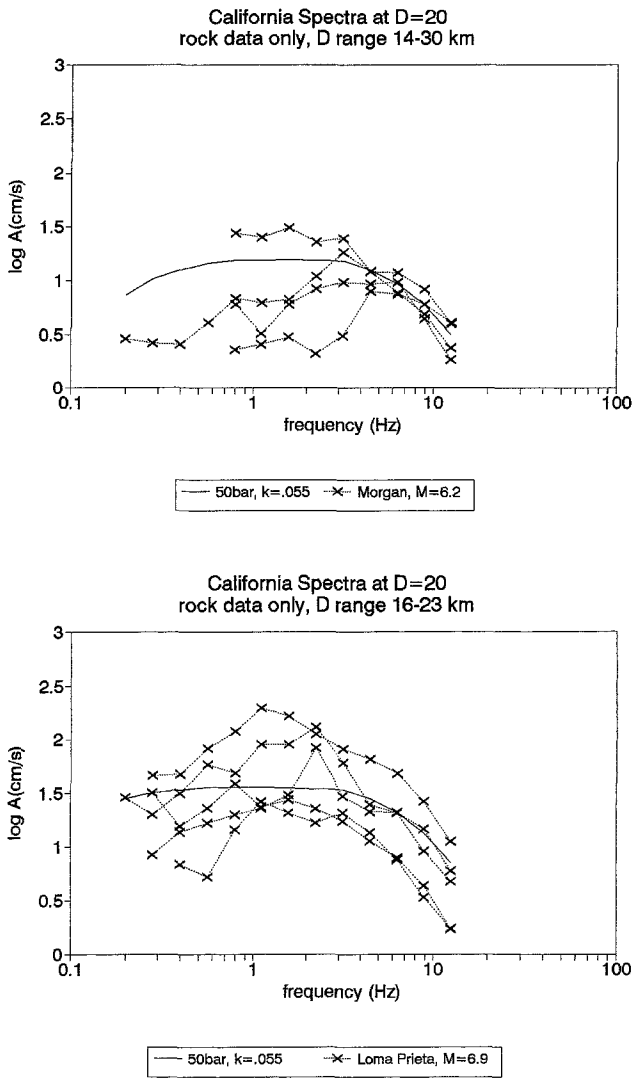

Figure 3. Fourier spectra for rock records at $D \cong 20$ km, for the M6.2 Morgan Hill earthquake (upper frame) and the M6.9 Loma Prieta earthquake (lower frame). Symbols are the smoothed amplitude values used in regressions. Solid line shows the 50-bar Brune point-source spectrum for the specified magnitude at $D = 20$ km, for kappa (κ_0) of 0.055 (chosen to match high-frequency shape of these two events).

1. $R \leqq R_{o1}$, where $R_{o1} = 50$ km (initial trial value), corresponding to attenuation of the direct wave;
2. $R_{o1} < R \leqq R_{o2}$, where $R_{o2} = 150$ km (initial trial value), corresponding to a transition zone as the direct wave is joined by postcritical reflections from mid-crustal interfaces and the Moho discontinuity; and
3. $R_{o2} < R$, corresponding to attenuation of multiply reflected and refracted S waves.

In the first iteration, all site terms are set equal to zero. For trial values R_{o1} and R_{o2}, we step through all plausible combinations of attenuation parameters, searching for the combination that minimizes the average residual error. The constraints imposed on b are that it be 1.0 or greater for the direct wave and 0.5 or greater for $R > R_{o2}$; it is unconstrained in the transition zone. The coefficient c is assumed to be frequency dependent; it has the same value in all three distance ranges. The frequency-dependent soil response terms are then obtained by averaging the residuals of the first iteration over all soil sites, under the constraint that the average log residuals on rock equal zero. These average soil terms are then input to a second iteration of the process. The solution converges very quickly, with little significant change occurring after the second iteration.

Possible nonlinearity of soil response was investigated by regressing the residuals against the predicted rock amplitudes. This finds the coefficients a and m for $\log S_j(f) = a + m \log A_{irx}$, where A_{irx} is the predicted rock amplitude for earthquake i at the distance corresponding to station j. The m coefficients, which express the degree of nonlinearity of the soil sites relative to the rock sites, were ambiguous. The m values were zero for low frequencies and had values in the range of 0.00 to -0.03 for frequencies greater than 1 Hz, with errors in the coefficient of 0.02 to 0.03. Therefore, the final soil terms (listed in the Appendix table) are treated as amplitude independent.

This does not necessarily mean that there is no nonlinearity in the soil response. The m values obtained from the regression would be consistent with a ratio as large as 1.4 for the linear versus nonlinear Fourier amplitude response factors, for the largest motions. Furthermore, it has been suggested that nonlinearity increases ground-motion duration, due to the amplitude dependence of shear-wave velocity (Marsh *et al.*, 1995). If this is so, then the response spectra may have amplitude-dependent soil response terms, even if the Fourier spectra do not. Finally, there may be nonlinearity in the response of the class A and B sites—although classified as rock, they are not very stiff, with near-surface shear-wave velocities of less than 350 m/sec on average (increasing to >600 m/sec within the upper 30 m). Any nonlinearity that included the sites classified as rock would be reflected in the source terms, since the rock response terms are zero by definition. Such nonlinearity would appear in the modeled kappa values, as discussed in the following section. Thus we can conclude only that the Fourier spectral data do not demand nonlinearity of the soil terms in the context of this regression scheme.

Attenuation Results

Initial investigations revealed that the attenuation curve has a trilinear shape similar to that reported by Campbell (1991) and Fletcher and Boatwright (1991) for the Loma Prieta earthquake, and by Atkinson and Mereu (1992) for ENA events. There is no resolved dependence of the geometric attenuation coefficient on frequency. The dataset can be described using $b = 1.0$ for $R \leqq 50$ km, $b = 0.0$ for $50 < R \leqq 170$ km, and $b = 0.5$ for $R > 170$ km. Due to the limited distance range of the data, the b coefficient is not well-constrained at $R > 100$ km. This causes ambiguity in

interpreting the shape of the attenuation curve but does not significantly affect the source or site terms: different potential choices of b are compensated by different solutions for $c(f)$, and there are sufficient data at close distances to constrain the source terms. In the final regressions, we set b = 1.0 for $R \leqq 50$ km, b = 0.0 for $50 < R \leqq 170$ km, and b = 0.5 for $R > 170$ km. For this trilinear geometric attenuation form, the associated solution for $c(f)$ implies $Q = 204\ f^{0.56}$ [where $Q = \pi f/(2.3\ c\beta)$].

Other choices of geometric attenuation provide as good a fit to the data and yield similar source terms; however, the associated solutions for $c(f)$ may not be consistent with typical regional Q models. For example, the data could be fit with a simple R^{-1} attenuation over all distances $R < 200$ km, but this would imply negative anelastic attenuation. Alternatively, the data could be fit to an R^{-1} form within 40 km, changing to an $R^{-1/2}$ form beyond; the $c(f)$ solution for this model implies $Q = 360\ f^{0.31}$, which is similar to the Q result obtained for the trilinear case. Both the bilinear and trilinear forms provide Q models in reasonable agreement with typical regional Q models for California, as determined from seismographic data (e.g., Chin and Aki, 1991). We conclude that the regressions cannot make a significant distinction between these two functional forms. This trade-off between geometric spreading and Q is common in attenuation studies (Atkinson, 1989; Frankel *et al.*, 1990). The selection of the trilinear over the bilinear form is thus somewhat arbitrary. This is not of great concern since our primary interest is in the source terms, which are approximately equal for the two attenuation models.

Initial regressions showed that the residuals in the near-source region greatly improve when the distance measure R includes a frequency-dependent "added depth" term, $h(f)$, determined by the regression; thus, we use

$$R = \sqrt{[D^2 + h(f)^2]}, \qquad (3)$$

where D is the closest distance to the rupture surface. The added depth term is analogous to that found by Boore *et al.* (1993) in their regression of the California response spectra database; it reflects the observation that high-frequency amplitudes "saturate" at near-source distances to a greater extent than do low-frequency amplitudes. (The term saturate means that the amplitudes approach a constant value as distance is decreased.) No resolved dependence of $h(f)$ on magnitude was found. The best-fit values of h are plotted versus frequency on Figure 4, along with an illustration of the effect of the h value on the shape of the attenuation curve. There is no obvious physical explanation for this frequency-dependent saturation effect. It might reflect a combination of effects: perhaps nonlinearity suppresses the high-frequency motions, while directivity enhances the long-period motions (W. Joyner, personal comm., 1996).

Figure 5 compares the model attenuation to data, for events of **M** 7 at frequencies of 0.28 and 4.5 Hz. The level of the model curve for **M** = 7 is set by the regression of

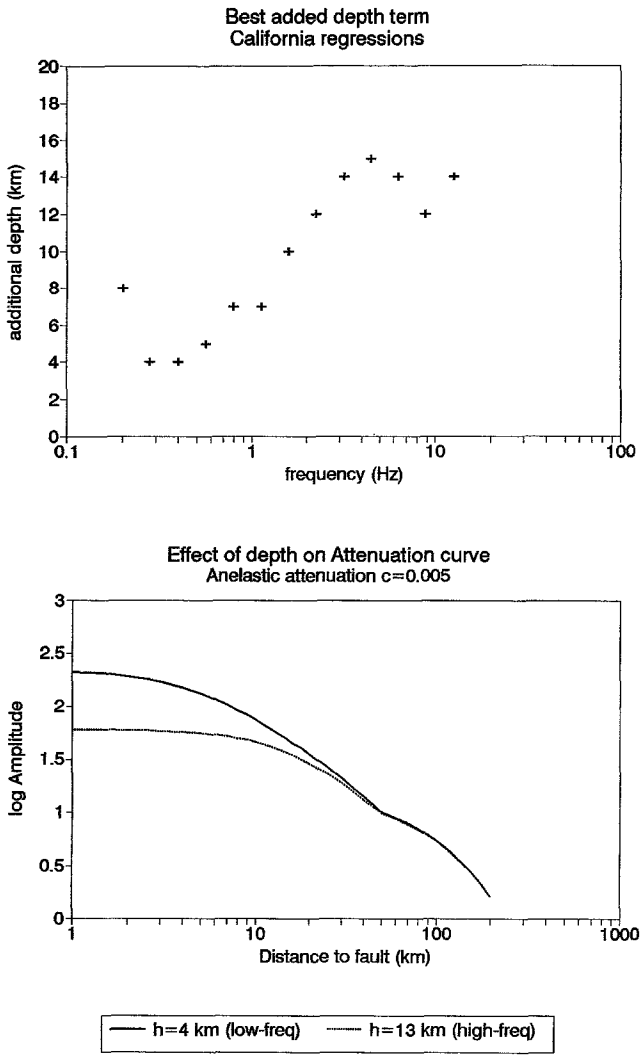

Figure 4. Depth terms $h(f)$ determined from regression analyses (top), and illustration of the effects of $h(f)$ on the shape of the attenuation curve (bottom).

source terms against **M**, as described in the next section. The data are not scaled, except for removal of the soil-response term ($-\log S_j$) for observations recorded on soil (class C/D). Simple R^{-1} attenuation, combined with a Brune point-source spectrum with stress parameter 50 and 100 bars, is also shown for reference (assumed focal depth = 8 km). Of course, it would also be reasonable to combine the Brune source model with a trilinear or bilinear attenuation form. In this case, the Brune model would agree more closely with the data for distances beyond 50 km (the Brune curves would then parallel the regression model curves, with the levels being set by the Brune source amplitudes). The main point of the figure is that the attenuation curves are well constrained by data in the distance range from 10 to 100 km and that the regression curve steers through the middle of the data cloud.

The standard deviation of the attenuation residuals (intraevent variability) is approximately 0.27 log units. This

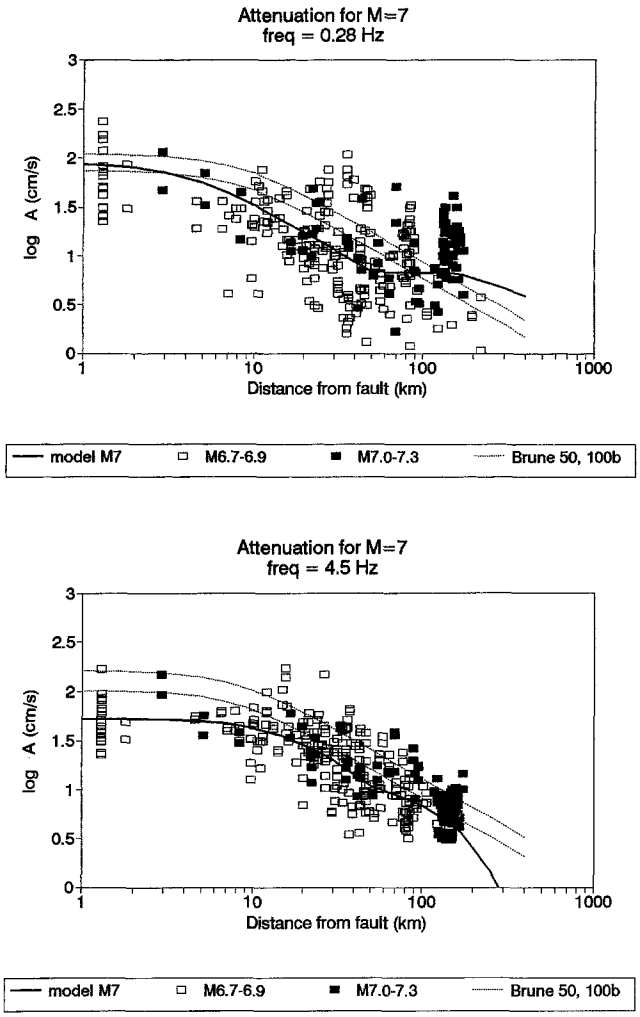

Figure 5. Attenuation model for an event of **M** = 7 (solid lines) at frequencies of 0.28 Hz (top frame) and 4.5 Hz (bottom frame), compared to data of **M** 6.7 to 7.3 (open squares for lower half of **M** range, filled squares for upper half of **M** range). Dotted lines show predictions of Brune point-source model with 50- and 100-bar stress parameters, for R^{-1} attenuation; depth of point source = 8 km. Note that other attenuation shapes (e.g., trilinear) could also be combined with the Brune source model, which would improve the fit of the Brune model to data at $D > 50$ km.

is considerably larger than the corresponding variability of 0.14 for ENA regressions of a hard-rock database (Atkinson and Mereu, 1992). The large variability is likely a consequence of the wide range in site conditions, as well as ambiguity in distance measures in applying a point-source model to extended rupture at close distances.

California Source Spectra

Regression Results from Empirical Data

The apparent shapes and amplitudes of California source spectra are determined by the terms A_{io} from the regression analysis (equation 2); A_{io} is the implied amplitude level for the reference distance $R = 1$ km. These terms are listed for each earthquake in the Appendix table; they implicitly include the amplification $V(f)$ by the near-surface crustal velocity gradient, as well as the effects of the average regional value of kappa for class A and B sites. It is important to keep this in mind when interpreting these terms as "source spectra."

Figure 6 displays the near-source amplitude (at $D = 10$ km) of each event as inferred from the source terms of the regression (e.g., $\log A_{D=10} = \log A_{oi} - \log R$, where $R = \sqrt{[10^2 + h(f)^2]}$), for three sample frequencies. To illustrate that these source amplitudes are robust with respect to the regression scheme, we also show alternative estimates of the average near-source amplitudes, obtained without the use of regression analyses, using the following simple procedure. From Figure 5, it is apparent that the data in the distance range from $D = 10$ to 60 km closely follow a simple D^{-1} attenuation. Therefore, we can scale all of the data in the distance range from 10 to 60 km back to $D = 10$ km by multiplying the amplitudes by $(D/10)$. To avoid the complication of soil response terms, we use only the "rock" (class A/B) data. The average for each event yields the "check" values shown on Figure 6. The close similarity in the trends for the regression results and the check values indicate that the regression source terms are robust. In fact, Figure 6 suggests that we do not even need to do a regression analysis to reach our conclusions regarding the source spectra; all we need to do is correct the rock data in the 10- to 60-km distance range back to $D = 10$. The regression model simply allows a broader range of data to be utilized and explored.

Figure 6 suggests that the source terms for each frequency can be satisfactorily modeled using a quadratic in **M**:

$$\log A_{io} = x_0 + x_1(\mathbf{M} - 6) + x_2(\mathbf{M} - 6)^2. \quad (4)$$

The Appendix table lists the least-squares coefficients of these equations, which implicitly include the effects of amplification by the crustal velocity gradient and near-surface attenuation by kappa for rock sites. Note that the quadratic equations for $\log A_{io}$ are not constrained to converge with the Brune-model spectra for frequencies on the "moment end" of the spectrum (i.e., low frequencies). This deficiency is potentially important for small-to-moderate events (**M** < 6) at $f \leqq 0.5$ Hz, which are poorly represented in the empirical database. An alternative two-corner formulation for the source terms that respects the moment constraint at low frequencies is shown on Figure 6 and discussed later.

The standard deviation of the source amplitudes about equation (4) (interevent variability) is approximately 0.22 log units at low frequencies, decreasing to 0.17 for $f \geqq 3$ Hz. The variability decreases significantly with increasing magnitude (from −0.2 at **M**5 to −0.1 at **M**7), implying that the source parameters of large earthquakes are less variable than those of small earthquakes. This is in agreement with

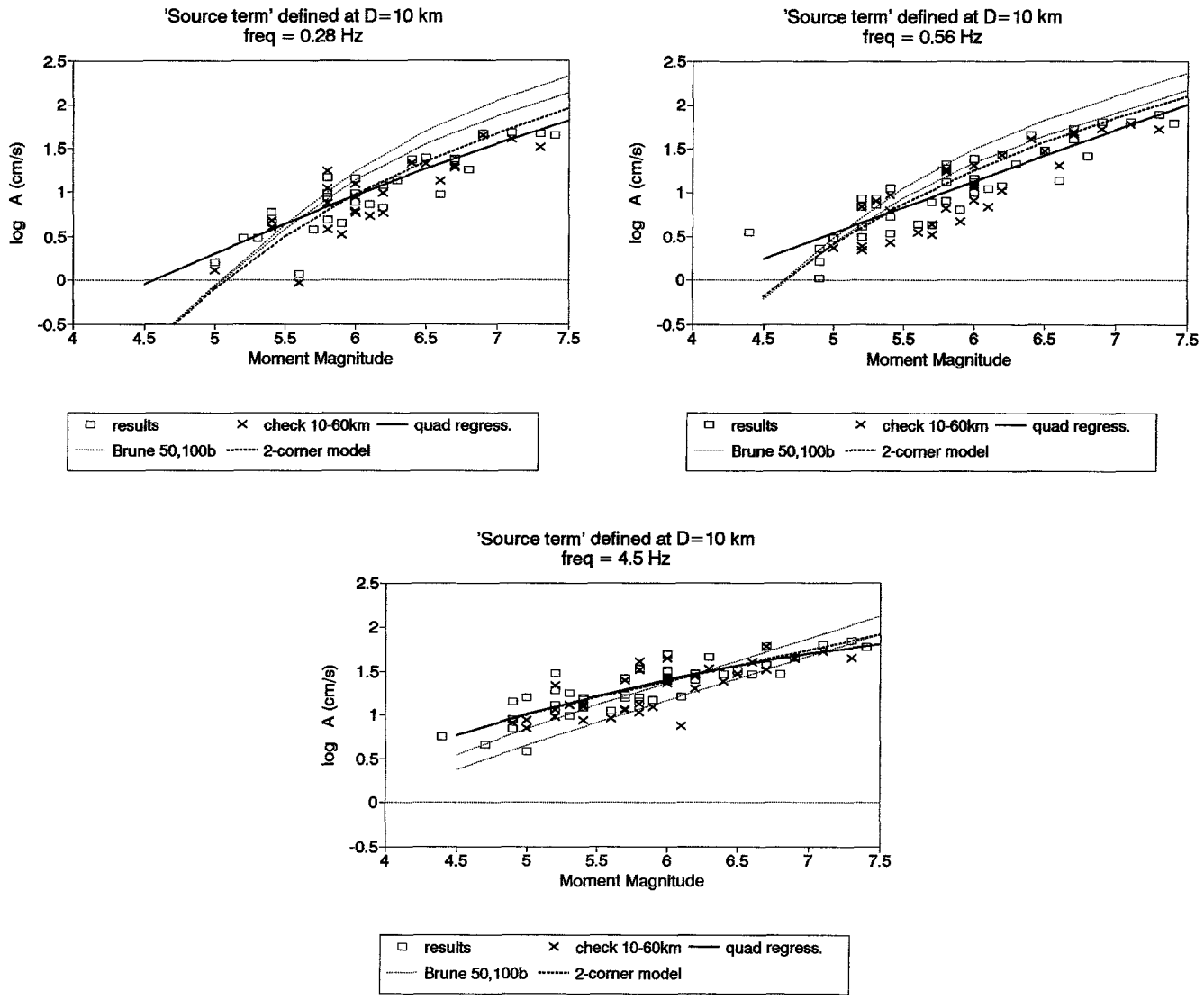

Figure 6. Source amplitudes for each event as obtained from regression, plotted for a reference distance of $D = 10$ km (open squares). X symbols show check values, obtained by correcting rock observations for each event, in the distance range $100 \leqq D \leqq 60$ km, back to $D = 10$ km (assuming D^{-1} attenuation). Solid lines show quadratic fit to source terms (equation 4). Light dotted lines show Brune point-source model values for 50- and 100-bar stress drops. Heavy dashed line shows empirical two-corner source model discussed in text (equations 7 through 10).

the results of previous studies (EPRI, 1993; Rydelek and Sacks, 1995). In the following section, the quadratic characterization of the source amplitudes (equation 4) will be used to compare the shape of the empirical source spectra to the predictions of the Brune point-source model and to those of a finite-fault model.

Finite-Fault Model of Spectra

The effects of a large finite source, including rupture propagation, directivity, and source-receiver geometry, can profoundly influence strong ground motions in terms of amplitude, frequency content, and duration. To accommodate these effects, a methodology that combines the aspects of finite-earthquake-source modeling techniques (Hartzell, 1978) with the stochastic point-source ground-motion model has been developed (Silva *et al.*, 1990; Silva and Stark, 1992; Schneider *et al.*, 1993). The approach is very similar to the empirical Green's function methodology introduced by Hartzell (1978) and Irikura (1983). In this case, however, the stochastic point-source is substituted for the empirical Green's function. Use of the stochastic point source as a Green's function is motivated by its demonstrated success in modeling strong ground motions (Hanks and McGuire, 1981; Boore, 1983, 1986; Silva and Stark, 1992; Schneider *et al.*, 1993).

For the finite-source characterization, a rectangular fault

is discretized into several subfaults, each of which is treated as a single point source. Heterogeneity of the earthquake source process is modeled by randomizing both the location of the subevents within each subfault (Hartzell, 1978) and the subevent rise time. Different values of slip are assigned to each subfault as relative weights, which allows for asperities or nonuniform slip. Random components are added to the assumed rupture velocity and to the computed radiation pattern for each subfault. The ground-motion time history at the receiver is computed by summing the contributions resulting from each of the subfaults. Crustal response effects are accommodated by using vertically or inclined propagating shear waves through the California velocity gradient model of Boore (1986). The simulations are computed for this generic rock profile assuming linear response, with a kappa value of 0.04 sec (Silva and Darragh, 1995). Wave propagation is treated with a simple R^{-1} attenuation model, with an assumed regional Q operator ($Q = 150 f^{0.6}$). The attenuation model is not critical since we are primarily interested in the near-source amplitudes. The resulting time history includes the salient features of rupture propagation and source finiteness, as well as gross propagation path and linear rock site effects.

To simulate a "generic" earthquake of specified moment magnitude, we assume a vertical strike-slip fault with area (km^2)

$$\log \text{area} = \mathbf{M} + 4.0 \tag{5}$$

and rise time

$$\log t = 0.33 \log M_0 - 8.62 \tag{6}$$

for M_0 in dyne-cm and t in seconds. Equation (5) was obtained by regression of the data listed in Wells and Coppersmith (1994), with the coefficient for **M** fixed at unity. Equation (6) approximates rise-time data, primarily from Heaton (1990), with the slope of the relation fixed at 0.33. The fault is discretized into subfaults, each of which has dimensions 3 by 3 km (**M**5 subevent); the implied subevent stress parameter, based on this area, is 30 bars. For the finite-fault simulations of this study, each simulated earthquake nucleates within a randomly drawn subfault; these hypocenters are constrained to be located in the bottom half of the rupture surface and within 10% of the fault ends. Rupture propagates in all directions with average velocity 0.8 β, where $\beta = 3.2$ km/sec.

A quantitative assessment of how well the finite-fault stochastic model describes observed ground motions has been made for the 1989 Loma Prieta (Schneider *et al.*, 1993) and 1987 Whittier Narrows earthquakes (Abrahamson *et al.*, 1990). The model bias, along with its 90% confidence limits, is shown in Figure 7. The model shows little or no bias from very high frequencies (peak ground acceleration) down to nearly 0.2 Hz (the limit of the useable data). This result suggests that the stochastic finite-fault model is a broadband

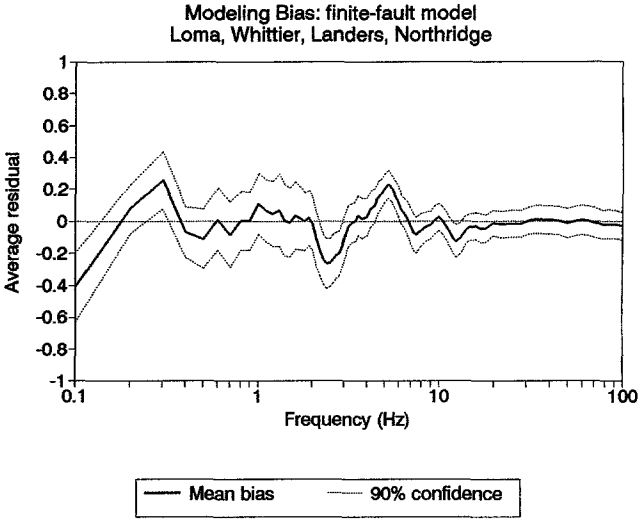

Figure 7. Model bias (e.g., average residual) for the stochastic finite-fault model, computed from the Loma Prieta, Whittier Narrows, Landers, and Northridge earthquakes, using 80 rock and soil sites [modified from Schneider *et al.* (1993) and Abrahamson *et al.* (1990)].

method with no apparent misfit for these earthquakes. The unbiased nature of the model lends confidence in its use to gain physical insight into the results of the empirical analyses.

In the real data set, the source spectra obtained from regression represent an average over a combination of fault orientations, slip distributions, and recording azimuths. To mimic these conditions, we average over a broad range of finite-fault simulations. Earthquakes of magnitude **M** 5.5, 6.5, and 7.5 are simulated. Fault lengths for these magnitudes are 6, 29, and 211 km, respectively, with widths of 5, 11, and 15 km, respectively. For each magnitude, motions are simulated at 11 points evenly spaced around the length of the fault, for 10 distances from 1 to 100 km. For each receiver location, we randomly generate 10 slip distribution. Thus, there are $3 \times 11 \times 10 \times 10 = 3300$ simulations in total.

The Fourier spectra of the simulated rock motions show considerable variability with azimuth and slip distribution, as shown on Figure 8. When averaged over all azimuths and slip distributions, as shown on Figure 9, the resulting spectra are fairly smooth; the degree of smoothness increases with increasing magnitude due to the averaging effects of a greater number of subsources.

Regression of the 3300 simulated spectra, using the same algorithm that was applied to the real data, confirms that the regression program correctly recovers the input attenuation form and that the source terms of the regression are consistent with the motions simulated at near-source distances ($D = 1$ km).

There are some features of the regression of the real data that are not present in the simulations. The simulated

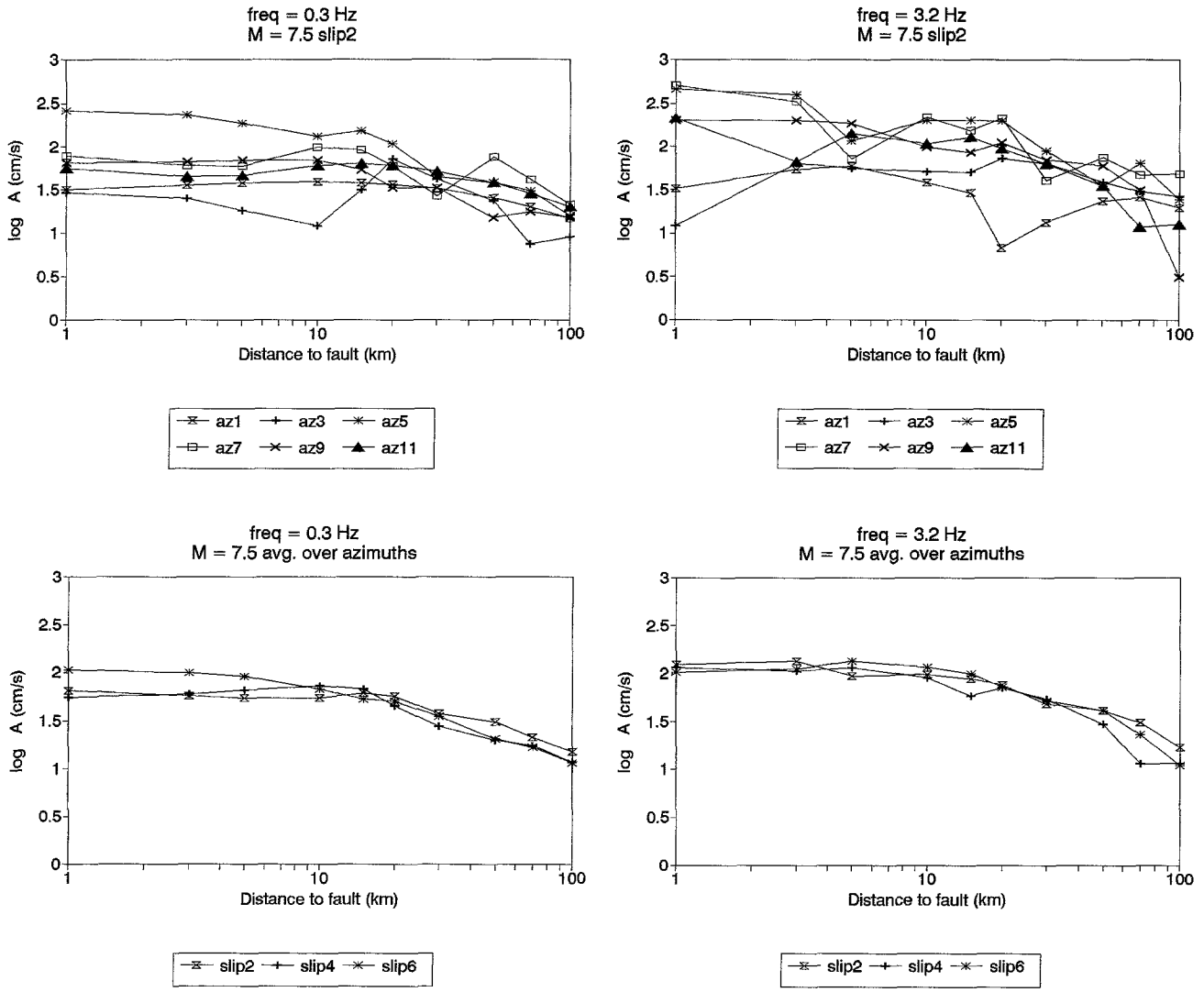

Figure 8. Fourier spectral amplitudes of simulated M7.5 earthquake at frequencies of 0.3 Hz (left) and 3.2 Hz (right) as a function of distance from the fault. Top frames show the dependence of amplitudes on azimuth, where az1 is at one end of the fault and az11 is at the opposite end, for one selected slip distribution. Bottom frames show the dependence of amplitudes on slip distribution, when averaged over all azimuths, for three selected slip distributions.

data require an added depth term to model saturation effects, but unlike the real data, this term is independent of frequency. The added depth term for the simulated data is 9 km for M5.5, 11 km for M6.5, and 17 km for M7.5 (or h = 11 overall). The increase of the apparent h with M is attributable to the greater fault width of the larger events. We infer that the frequency dependence of h in the real data reflects unmodeled effects, such as nonlinearity.

Comparison of Empirical Data to Models

We wish to compare the shape and amplitudes of the empirical source spectra for California earthquakes to the predictions of the Brune point-source model and the stochastic finite-fault model. The Brune point-source spectra require specification of the stress parameter and kappa. Kappa is generally considered a site parameter rather than a source parameter (Anderson and Hough, 1984; Silva and Darragh, 1995). Nevertheless, it appears in the average empirical source shape determined for rock sites, because the regression assumes that rock sites have an average amplification of 1.0 for each frequency. (Whether kappa is cast into the source or site terms is simply a matter of bookkeeping and does not affect the overall conclusions of the regressions.) To compare our regression results with the point-source model, we first determine the average kappa value implied by the empirical source spectrum. This is done by fitting a straight line to the log spectral amplitude versus frequency for all frequencies greater than that for which the high-frequency level is attained (e.g., for $f > 2f_o$, where f_o is the corner frequency of the Brune spectrum). The stress

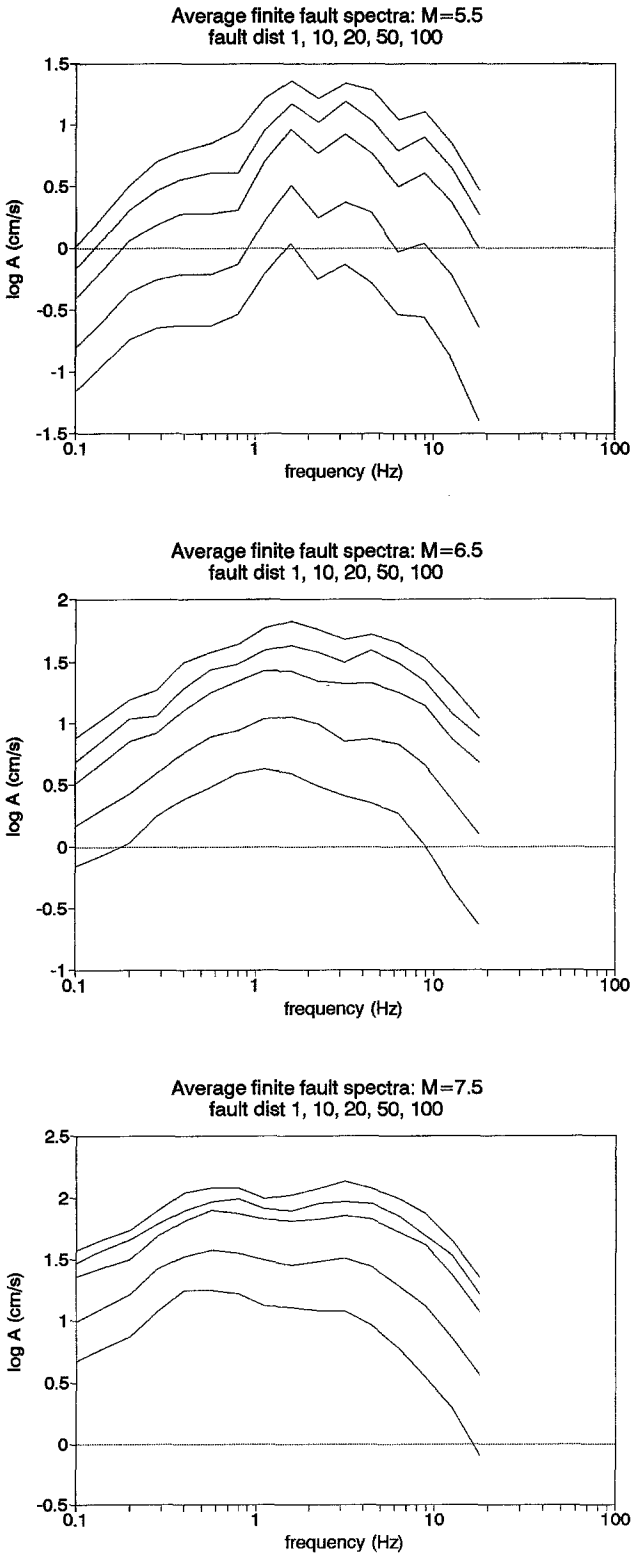

Figure 9. Fourier spectra of finite-fault simulations, averaged over all azimuths and slip distributions, at distances of 1, 10, 20, 50, and 100 km from the fault, for earthquakes of M5.5 (top), M6.5 (middle), and M7.5 (bottom).

parameter is then determined as that value of $\Delta\sigma$ required by equation (1) to match the high-frequency spectral level, accounting for the effects of crustal amplification and kappa (κ_0). Using this procedure, the empirical spectrum for M5.5 would indicate a Brune stress of $\Delta\sigma$ = 120 bars and κ_0 = 0.035 sec. For M6.5, we would infer $\Delta\sigma$ = 90 bars and κ_0 = 0.045 sec, while for M7.5 $\Delta\sigma$ = 50 bars and κ_0 = 0.05 sec. There is some arbitrariness in these parameters due to the strong trade-off between $\Delta\sigma$ and κ (Anderson, 1986; Boore *et al.*, 1992). Note that an increase in kappa with increasing magnitude may be interpreted as evidence of nonlinearity of strong ground motion for typical California site conditions. The apparent decrease in $\Delta\sigma$ with increasing M may reflect saturation effects attributable to the point-source distance measure and is not necessarily indicative of real stresses on the fault surface.

Figure 10 compares the source terms from the regression of the empirical data to the predictions of the Brune point-source model and the stochastic finite-fault model. The comparisons are made at a reference distance of R = 8 km (near the minimum value of R for observations on the surface). The actual value of R used in the comparisons is arbitrary as it simply scales all curves up or down. Use of a reference R rather than a reference D does influence the shape of the curves, through the frequency dependence of the added depth term (recall $R = \sqrt{[D^2 + h(f)^2]}$). By plotting the comparisons for a reference R, we display the far-field shape of the spectrum. As the source is approached (D < 10 km), the high-frequency amplitudes saturate more quickly than do the low-frequency amplitudes, which mitigates the apparent spectral sag.

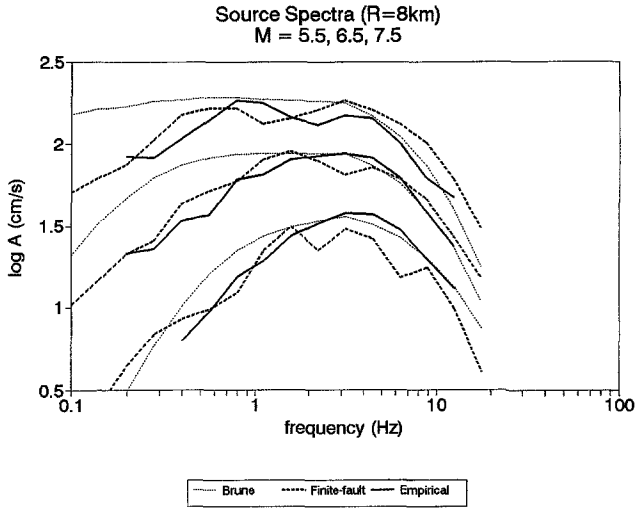

Figure 10. Source terms A_{io} from regression of empirical data, as fit by equation (4) for M5.5, 6.5, and 7.5 (solid lines). Light dotted lines show corresponding Brune point-source predictions for stress parameters of 120, 90, and 50 bars, respectively, while heavy dashed lines show corresponding stochastic finite-fault predictions.

At the high-frequency end of the spectrum ($f \geqq 1$ Hz), both the point-source and the finite-fault model spectra match the empirical source spectra. For frequencies less than 1 Hz, by contrast, the empirical source spectra have significantly lower spectral amplitudes than predicted by the Brune point-source model; the discrepancy increases with decreasing frequency, and with increasing magnitude.

The finite-fault stochastic model shows the same features as the empirical spectra, relative to the point-source model. The finite-fault predictions track the empirical source spectra quite well over all frequencies from 0.2 to 12 Hz. This is strong evidence that empirical source spectra require a model that is more complex than the single-corner point source, for earthquakes greater than about **M**5.5. Significantly, this complexity in spectral shape is a predictable result of the finite-fault modeling. Similar deductions regarding spectral shape were made by Gusev (1983) based on global magnitude measures for very large earthquakes, by Boatwright and Choy (1992) for intraplate earthquakes, and by Atkinson (1993) for ENA events. We conclude that the observed departure from the single-corner-frequency source model may be a stable feature of large earthquakes.

Discussion

The deviations of the empirical source spectra from the predictions of the Brune point source, at frequencies of $f \leqq 1$ Hz, are similar to those inferred by Atkinson (1993) for earthquakes in ENA, based on data sources less direct than those used in this study. It is interesting to compare the California source spectra to the empirical model developed for ENA. To isolate the relative differences in ground motion attributable to source processes, we make corrections to the ENA empirical source spectra so as to place them in the California crust. This involves accounting for the effects of amplification through the California crustal velocity gradient and near-surface damping through kappa. We may also consider the effects of differing material properties in the source region, as these scale the spectral amplitudes (see equations 1 and 7). Figure 11 shows the effect of these corrections. To account for the effects of the weathered rock layer near the Earth's surface in California, the ENA hard-rock spectra are multiplied by the California crustal amplification factors of Boore (1986) (Appendix table) and by the factor $\exp(-\pi\kappa_0 f)$, using the California rock kappa values of this study. This modifies the shape of the ENA spectra so that it is comparable to the California shape for moderate events. If we also account for the different shear-wave velocities in the near-source region for the standard crustal models used (3.8 km/sec in ENA versus 3.2 km/sec in California), this scales the ENA spectra up to the final position labeled "ENA in CA crust" on Figure 11. We note that this latter correction (a factor of 1.67) may be too large if actual differences in mid-crustal velocities are more modest than those assumed here; for example, the EPRI (1993) crustal model for ENA uses a near-source velocity of 3.6 km/sec, while recent updates to the California crustal model use a mid-crustal velocity of 3.5 km/sec (Boore, personal comm., 1996).

Subject to the assumptions outlined above, Figure 11 suggests that the ENA and California source spectra are similar in amplitude for low frequencies ($\leqq 1$ Hz). The ENA earthquakes appear to have elevated high-frequency levels, at least for hard-rock sites, compared to the California source spectra. The discrepancy is modest for moderate events but quite dramatic for large earthquakes. Bear in mind that for ground motions observed on the surface, this is mitigated by the higher near-source velocities and the relative lack of amplification through the ENA crustal profile (i.e., lines labeled ENA on ENA rock on Fig. 11). The comparison is consistent with the inference that ENA stress parameter values average 150 to 200 bars, independent of magnitude (Atkinson, 1993), while California stress parameters appear to decrease with magnitude from about 120 bars at **M**5.5 to only 50 bars at **M**7.5.

The large discrepancy between the California and ENA high-frequency source levels at large magnitudes is intriguing. This may be a result of real differences in stress released during large events: it has been suggested that stress drops are related to the repeat time of large events, such that infrequent large events on well-healed fault zones might be characterized by higher stress, perhaps due to a greater density of strong asperities (e.g., Kanamori and Anderson, 1975; Kanamori and Allen, 1986). Alternatively, the apparent differences in stress may be an artifact of other processes, such as pervasive nonlinearity of strong ground motion at typical California sites. Finally, and perhaps most significantly, the data for large events in ENA are extremely sparse, raising the possibility that the ENA source spectra may be overpredicted for large magnitudes. This latter possibility is perhaps tempered by the fact that the best-recorded large ENA event, the 1988 Saguenay earthquake of **M**5.8, clearly had high-frequency spectral levels greatly exceeding corresponding California source spectra for events of similar magnitude (Hough *et al.*, 1989; Boore and Atkinson, 1992). By contrast, though, the 1985 Nahanni earthquake of **M**6.8, widely regarded as an intraplate event, had relatively modest high-frequency ground motions (Boore and Atkinson, 1989). It is possible that a partial explanation for the differences between ENA and California source spectra may lie in the apparently larger variability of ENA stress parameters (Atkinson and Hanks, 1995). On the other hand, the apparent difference in stress variability may be an artifact of the magnitude range available for analysis, as the variability in source amplitudes decreases with increasing magnitude. Further study of the processes driving the apparent differences in source spectra is needed before definitive conclusions can be drawn.

The ENA source spectra were modeled using a form representing the superposition of Brune point-source spectra (Atkinson, 1993):

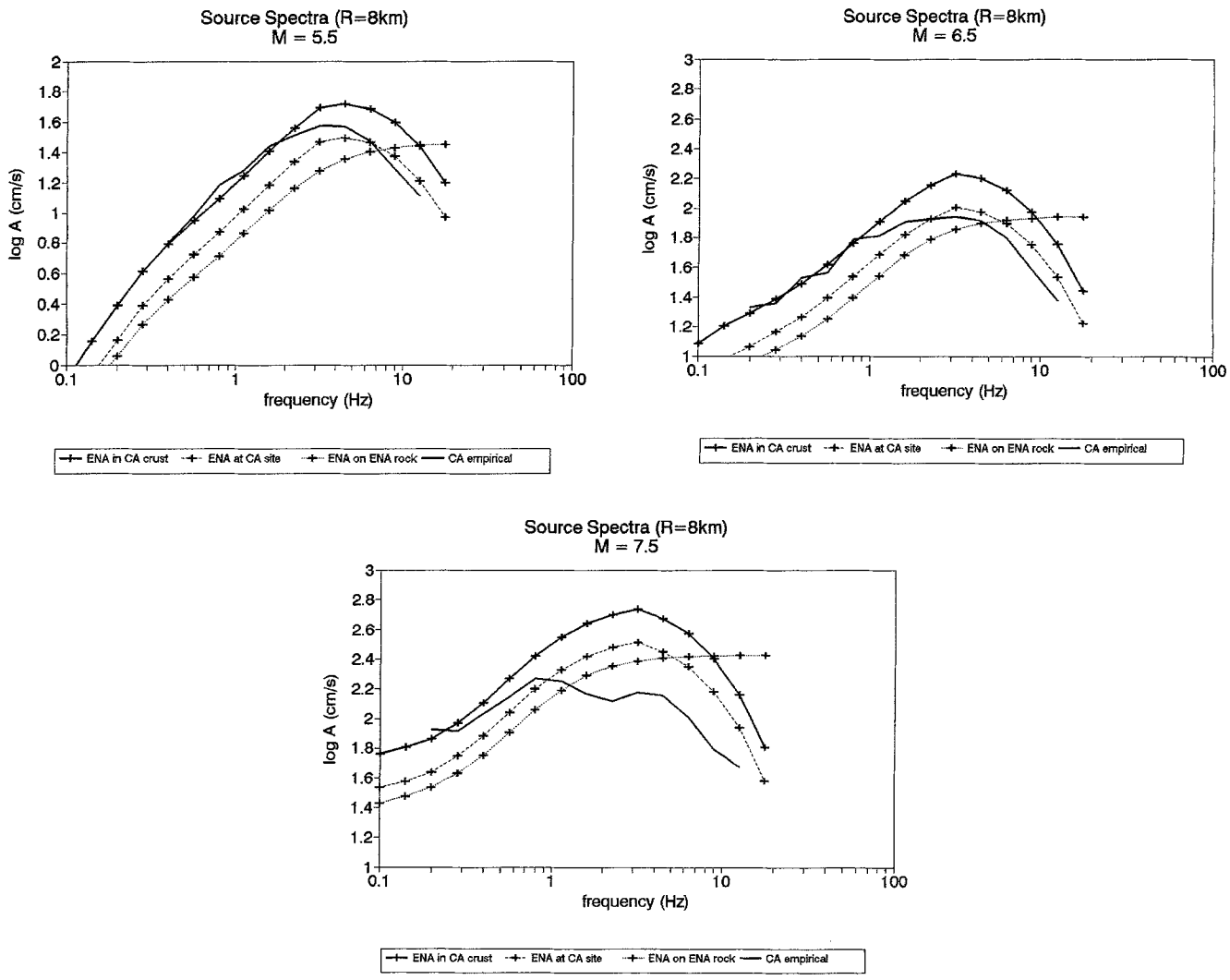

Figure 11. Comparison of empirical California source spectra (heavy solid lines) with ENA source spectra that have been adjusted to represent California crustal and site conditions (heavy solid lines with symbols). Uncorrected values for ENA surface observations for hard-rock sites are indicated by dotted lines with symbols. Dashed lines with symbols show first step of adjustment to ENA spectra, accounting just for California site conditions (no adjustment for mid-crustal velocities). Comparison shown for M5.5 (top left), M6.5 (top right), and M7.5 (bottom).

$$A_o(f) = C(2\pi f)^2 M_0 \{(1 - \varepsilon)/[1 + (f/f_A)^2] + \varepsilon/[1 + (f/f_B)^2]\}, \quad (7)$$

where C is as defined for equation (1) (but with $\mathcal{P} = 2.8$ g/cm^3 and $\beta = 3.8$ km/sec for ENA), f_A and f_B are the lower and upper corner frequencies of the source spectrum, and ε takes a value between 0 (point source with corner f_A) and 1 (point source with corner f_B). In this form, any modifications of the source spectra through the crustal velocity gradient or kappa are not included. Thus, we must remove any such effects before determining the parameters f_A, f_B, and ε from empirical observations. The form is rather arbitrary in the sense that it has no physical derivation; however, it conveniently casts the spectra in terms of observable spectral parameters f_A and f_B (rather than requiring a large number of frequency-dependent quadratic coefficients, as used in the Appendix table), and it appears to represent the observed shape over a very broad frequency range. The addition of only two Brune sources in the functional form is a convenient simplification of the concept of summation; similar shapes are obtained if a greater number of point sources, with corners lying between f_A and f_B, are summed in a more complex manner.

The California spectra can be represented by equation (7) by defining the parameters f_A, f_B, and ε, following a similar approach as that used for ENA. The lower corner is given by $1/(2T)$, where T is the source duration (Boatwright and Choy, 1992). The values of f_A inferred from source duration data compiled for California earthquakes (Somerville *et al.*, 1987; Kawase and Aki, 1990; Steidl *et al.*, 1991; Wald and

Heaton, 1994), as plotted in Figure 12, can be described as a function of magnitude by

$$\log f_A = 2.181 - 0.496\,\mathbf{M} \qquad (8)$$

with a standard error of 0.18 log units.

The upper corner frequencies can be determined from the source terms of the regression analysis (corrected for crustal factors as described above); for consistency with the Brune model, the value of f_B is the frequency at which the source spectrum attains 1/2 of its high-frequency amplitude level. As shown in Figure 12, this corner is given by

$$\log f_B = 1.778 - 0.302\,\mathbf{M} \qquad (9)$$

with a standard error of 0.19 log units.

The remaining parameter, ε, is determined from the source terms so as to minimize the average misfit to equation (7), for f_A values as given by equation (8) with f_B values determined from the source spectra. As shown in Figure 12, the parameter is fitted by

$$\log \varepsilon = 2.764 - 0.623\,\mathbf{M}, \qquad (10)$$

but with a rather large standard error of 0.43 log units.

Figure 12 also compares the California values of parameters f_A, f_B, and ε to the corresponding ENA values inferred by Atkinson (1993) based on limited ENA data. The parameter values determined from the simulated finite-fault spectra are also shown (but were not used in the fits); the f_A values for the simulations are based on the rupture duration for bilateral rupture, while the f_B and ε values are determined for each slip distribution from regressions of the simulated data. There are apparently no significant differences between ENA and California in terms of the corner frequencies f_A and f_B. The higher values of f_B and lower values of ε used in the ENA model were required to match the large ENA spectral levels at high frequencies, relative to those at lower frequencies.

Figure 13 compares the two-corner spectral form to the quadratic frequency-dependent form, and to the Brune and finite-fault model predictions (see also Fig. 6). It follows the quadratic empirical predictions quite closely, considering the more limited number of coefficients. To apply equation (7) to ground-motion predictions, the source amplitudes A_o (f) must be multiplied by the California crustal amplifications (Appendix table) and the factor $\exp(-\pi k_0 f)$. Kappa may be magnitude dependent, or given by an average value such as 0.04 sec. The spectra are then attenuated to the observation distance R using the trilinear attenuation form. Application of these steps will reproduce the average empirically observed Fourier spectral levels. (Note that if different crustal amplification factors or a different attenuation model than those of this study are used in the process, then the empirical observations will not be reproduced, unless the parameters

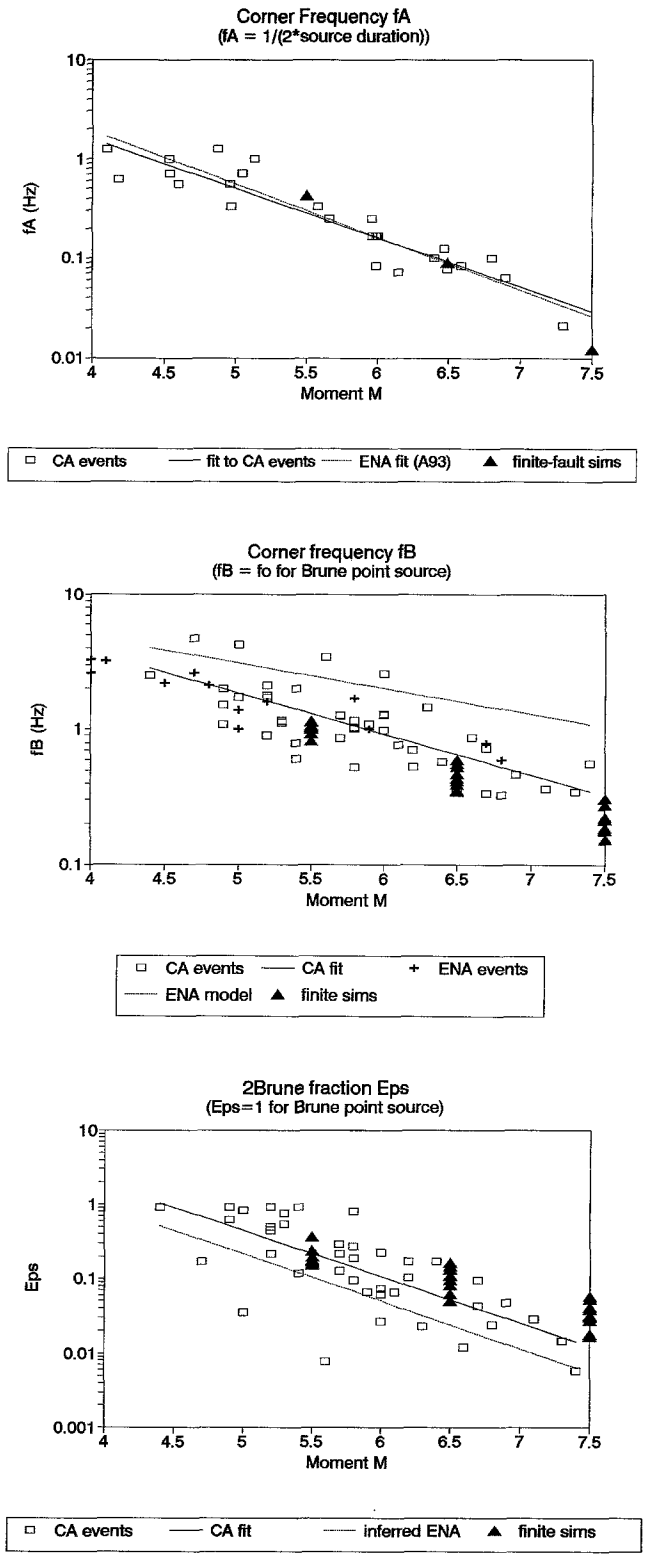

Figure 12. Parameters f_A (top), f_B (middle), and ε (bottom) of two-Brune characterization of source spectra (equation 7). Open squares show California data, plus symbols show ENA data, and filled triangles show values inferred from finite-fault simulations. Solid lines show least-squares fits to California data points (excluding simulations); dotted lines show ENA fits or model.

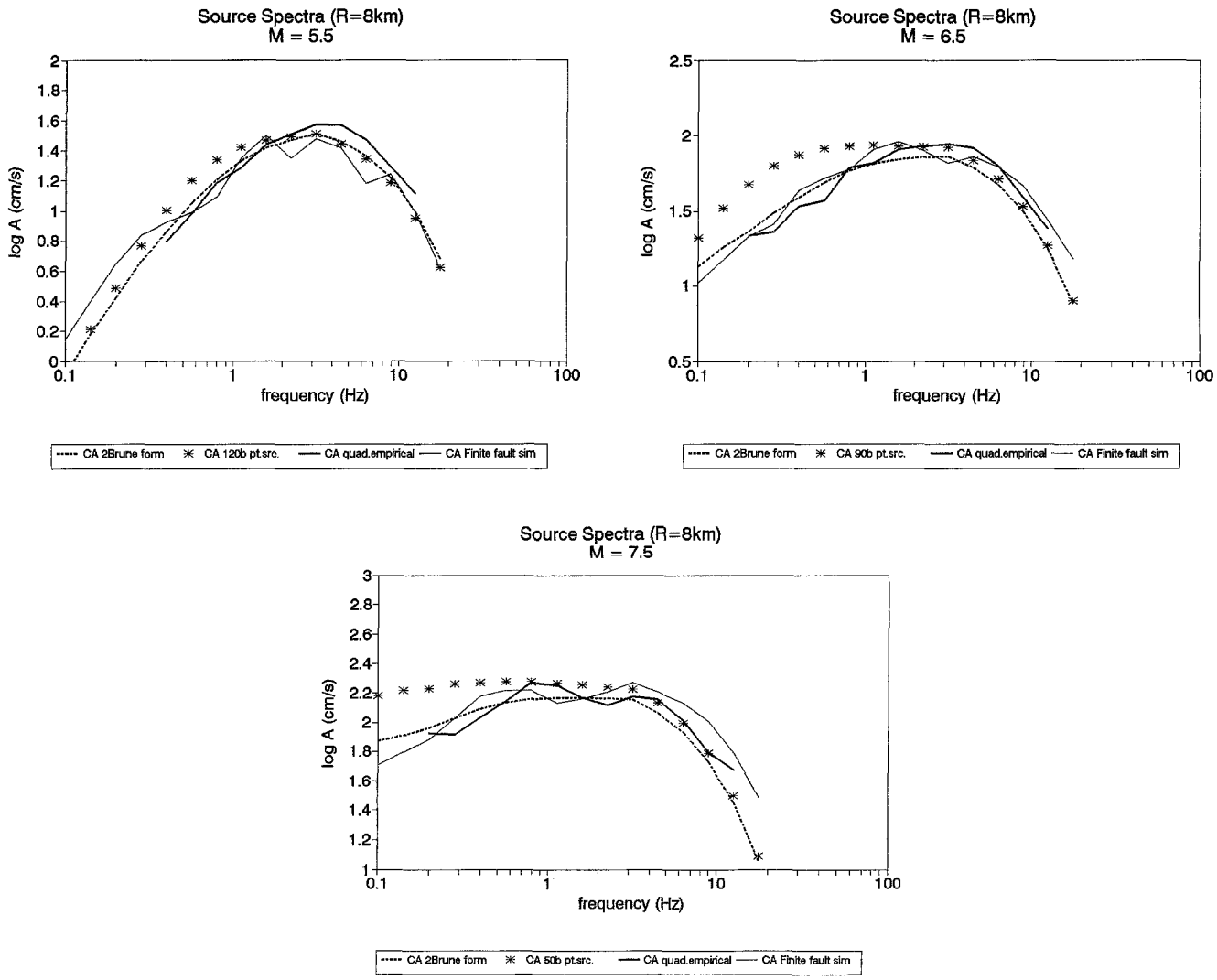

Figure 13. Comparison of the two-Brune characterization of source spectra (equation 7), after corrections to include crustal amplification effects (dashed lines), with the quadratic form of the empirical data (heavy solid lines) and the point-source (symbols) and finite-fault (light solid lines) predictions. Comparisons are made for **M**5.5 (top left), **M**6.5 (top right), and **M**7.5 (bottom). Point-source model uses magnitude-dependent stress and kappa (see text).

of equation (7) are first recomputed to reflect these different assumptions.)

Conclusions

Empirically derived source spectra for California earthquakes are generally inconsistent with the spectral shape implied by a Brune point-source model at low frequencies ($f \leqq 1$ Hz) and for large magnitudes (**M** $\geqq$ 6.5). This is manifested by magnitude and frequency dependence of the Brune model parameters. At high frequencies, the Brune stress parameter that best matches the data decreases from a value of about 120 bars at **M**5.5 to a value near 50 bars at **M**7.5. This may reflect saturation effects attributable to the point-source distance measure, rather than real stresses on the fault. At frequencies less than 1 Hz, the Brune single-corner point-source model overpredicts the source spectra. The discrepancy grows with decreasing frequency and with increasing magnitude. Finite-fault simulations indicate that this may be a consequence of the breakdown of the validity of the single-corner point-source approximation for large finite ruptures. A stochastic finite-fault model, in which the fault is discretized as a number of subfaults, each of which is represented by a Brune single-corner point source, correctly matches the observed spectral shapes and amplitudes.

The spectral decay parameter kappa, representing average near-surface attenuation of high-frequency motion at soft-rock sites, increases with increasing magnitude, from values near 0.035 sec at **M**5.5 to 0.050 sec at **M**7.5. This may be interpreted as evidence of nonlinearity for typical California sites subjected to strong ground motion.

For equivalent crustal conditions, empirical source spectra for California are similar in amplitude to corresponding spectra for ENA for low-frequency motions ($f < 2$ Hz for M5.5, $f < 0.5$ Hz for M7.5). The ENA events appear to have enhanced high-frequency levels not present in the California data; this may be particularly pronounced for large-magnitude earthquakes.

Acknowledgments

This work was funded by the National Earthquake Hazards Reduction Program, administered by U.S. Geological Survey under Contract 1434-95-G-2521. The Electric Power Research Institute funded reprocessing of the earthquake data. We benefited from stimulating discussions and comments from Norm Abrahamson, Dave Boore, and Bill Joyner. Tom Hanks prodded us to provide a clearer presentation and discussion of the analysis and results.

References

Abrahamson, N., P. Somerville, and A. Cornell (1990). Uncertainty in numerical strong motion predictions. *Proceedings of the Fourth National Conference on Earthquake Engineering,* Palm Springs, California, Vol. 1, 407–416.

Anderson, J. (1986). Implication of attenuation for studies of the earthquake source, in *Earthquake Source Mechanics,* S. Das, J. Boatwright, and C. H. Scholz (Editors), American Geophysical Monograph **37,** 311–318.

Anderson, J. and S. Hough (1984). A model for the shape of the Fourier amplitude spectrum of acceleration at high frequencies, *Bull. Seism. Soc. Am.* **74,** 1969–1993.

Atkinson, G. (1989). Attenuation of the Lg phase and site response for the Eastern Canada Telemetred Network, *Seism. Res. Lett.* **60,** no. 2, 59–69.

Atkinson, G. (1993). Source spectra for earthquakes in eastern North America, *Bull. Seism. Soc. Am.* **83,** 1778–1798.

Atkinson, G. and D. Boore (1995). New ground motion relations for eastern North America, *Bull. Seism. Soc. Am.* **85,** 17–30.

Atkinson, G. and T. Hanks (1995). A high-frequency magnitude scale, *Bull. Seism. Soc. Am.* **85,** 825–833.

Atkinson, G. and R. Mereu (1992). The shape of ground motion attenuation curves in southeastern Canada, *Bull. Seism. Soc. Am.* **82,** 2014–2031.

Atkinson, G. and P. Somerville (1994). Calibration of time history simulation methods, *Bull. Seism. Soc. Am.* **84,** 400–414.

Boatwright, J. and G. Choy (1992). Acceleration source spectra anticipated for large earthquakes in northeastern North America, *Bull. Seism. Soc. Am.* **82,** 660–682.

Boore, D. (1983). Stochastic simulation of high-frequency ground motions based on seismological models of the radiated spectra, *Bull. Seism. Soc. Am.* **73,** 1865–1894.

Boore, D. (1986). Short-period P- and S-wave radiation from large earthquakes: implications for spectral scaling relations, *Bull. Seism. Soc. Am.* **76,** 43–64.

Boore, D. and G. Atkinson (1989). Spectral scaling of the 1985–1988 Nahanni, Northwest Territories, earthquakes, *Bull. Seism. Soc. Am.* **79,** 1736–1761.

Boore, D. and G. Atkinson (1992). Source spectra for the 1988 Saguenay, Quebec earthquakes, *Bull. Seism. Soc. Am.* **82,** 683–719.

Boore, D., W. Joyner, and T. Fumal (1993). Estimation of response spectra and peak accelerations from western North American earthquakes: an interim report, *U.S. Geol. Surv. Open-File Rept. 93–509.*

Boore, D., W. Joyner, and L. Wennerberg (1992). Fitting the stochastic omega-squared source model to observed response spectra in western North America: trade-offs between stress drop and kappa, *Bull. Seism. Soc. Am.* **82,** 1956–1963.

Brune, J. (1970). Tectonic stress and the spectra of seismic shear waves from earthquakes, *J. Geophys. Res.* **75,** 4997–5009.

Brune, J. (1971). Correction, *J. Geophys. Res.* **76,** 5002.

Campbell, K. (1991). An empirical analysis of peak horizontal acceleration for the Loma Prieta, California, earthquake of 18 October 1989, *Bull. Seism. Soc. Am.* **81,** 1838–1858.

Chin, B. and K. Aki (1991). Simultaneous study of the source, path and site effects on strong ground motion during the 1989 Loma Prieta earthquake: a preliminary result on pervasive nonlinear site effects, *Bull. Seism. Soc. Am.* **81,** 1859–1884.

EPRI (1993). Guidelines for determining design basis ground motions. Early site permit demonstration program, Vol. 1, RP3302, Electric Power Research Institute, Palo Alto, California.

Fletcher, J. and J. Boatwright (1991). Source parameters of Loma Prieta aftershocks and wave propagation characteristics along the San Francisco Peninsula from a joint inversion of digital seismograms, *Bull. Seism. Soc. Am.* **81,** 1783–1812.

Frankel, A., A. McGarr, J. Bicknell, J. Mori, L. Seeber, and E. Cranswick (1990). Attenuation of high-frequency shear waves in the crust: measurements from New York State, South Africa, and southern California, *J. Geophys. Res.* **95,** no. B11, 17441–17457.

Gusev, A. (1983). Descriptive statistical model of earthquake source radiation and its application to an estimate of short-period strong motion, *Geophys. J. R. Astr. Soc.* **74,** 787–808.

Hanks, T. and R. McGuire (1981). The character of high-frequency strong ground motion, *Bull. Seism. Soc. Am.* **71,** 2071–2095.

Hartzell, S. (1978). Earthquake aftershocks as Green's functions, *Geophys. Res. Lett.* **5,** 1–14.

Hartzell, S. and J. Brune (1979). The Horse Canyon earthquake of August 2 1975—Two-stage stress-release process in a strike-slip earthquake, *Bull. Seism. Soc. Am.* **69,** 1161–1173.

Hartzell, S. and T. Heaton (1986). Rupture history of the 1984 Morgan Hill, California, earthquake from the inversion of strong motion records, *Bull. Seism. Soc. Am.* **76,** 649–674.

Hartzell, S. and M. Iida (1990). Source complexity of the 1987 Whittier Narrows, California, earthquake from the inversion of strong motion records, *J. Geophys. Res.* **95,** 12475–12485.

Heaton, T. (1990). Evidence for and implications of self-healing pulses of slip in earthquake rupture, *Phys. Earth Planet. Interiors* **64,** 1–20.

Hough, S. and D. Dreger (1995). Source parameters of the 23 April 1992 M 6.1 Joshua Tree, California, earthquake and its aftershocks: empirical Green's function analysis of GEOS and TERRAscope data, *Bull. Seism. Soc. Am.* **85,** 1576–1590.

Hough, S., K. Jacob, and P. Friberg (1989). The 11/25/88, M = 6 Saguenay earthquake near Chicoutimi, Quebec: evidence for anisotropic wave propagation in northeastern North America, *Geophys. Res. Lett.* **16,** 645–648.

Irikura, K. (1983). Semi-empirical estimation of strong ground motions during large earthquakes, *Bull. Disaster Prevention Res. Inst. Kyoto Univ.* **33,** 63–104.

Kanamori, H. and C. Allen (1986). Earthquake repeat time and average stress drop, in *Earthquake Source Mechanics,* S. Das, J. Boatwright, and C. H. Scholz (Editors), American Geophysical Monograph 37, Washington, D.C.

Kanamori, H. and D. Anderson (1975). Theoretical basis of some empirical relations in seismology, *Bull. Seism. Soc. Am.* **65,** 1073–1095.

Kawase, H. and K. Aki (1990). Topography effect at the critical SV-wave incidence: possible explanation of damage pattern by the Whittier Narrows, California, earthquake of 1 October 1987, *Bull. Seism. Soc. Am.* **80,** 1–22.

Marsh, J., T. Larkin, A. Haines, and R. Benites (1995). Comparison of linear and nonlinear seismic responses of two-dimensional alluvial basins, *Bull. Seism. Soc. Am.* **85,** 874–889.

Papageorgiou, A. and K. Aki (1983). A specific barrier model for the quantitative description of inhomogeneous faulting and the prediction of strong ground motion. Part I. Description of the model, *Bull, Seism. Soc. Am.* **73,** 693–722.

Savage, J. (1972). Relation of corner frequency to fault dimensions, *J. Geophys. Res.* **77,** 3788–3795.

Schneider, J., W. Silva, and C. Stark (1993). Ground motion model for the 1989 M 6.9 Loma Prieta earthquake including effects of source, path and site, *Earthquake Spectra* **9,** 251–287.

Silva, W. (1992). Factors controlling strong ground motions and their associated uncertainties, *ASCE Symposium on High Level Nuclear Waste Repositories,* 132–161.

Silva, W. and R. Darragh (1995). Engineering characterization of earthquake strong ground motion recorded at rock sites. Electric Power Research Inst., Report TR-102261, Palo Alto, California.

Silva, W., R. Darragh, and I. Wong (1990). Engineering characterization of earthquake strong ground motions with applications to the Pacific Northwest, in Hays, W., ed., Proceedings at the Third NEHRP Workshop on Earthquake hazards in the Puget Sound/Portland Region, W. Hays (Editor), *U.S. Geol. Surv. Open-File Rept.*

Silva, W. and C. Stark (1992). Source, path, and site ground motion model for the 1989 M 6.9 Loma Prieta earthquake, CDMG report.

Somerville, P., J. McLaren, L. Lefevre, R. Burger, and D. Helmberger (1987). Comparison of source scaling relations of eastern and western North American earthquakes, *Bull. Seism. Soc. Am.* **77,** 322–346.

Steidl, J., R. Archuleta, and S. Hartzell (1991). Rupture history of the 1989 Loma Prieta, California, earthquake, *Bull. Seism. Soc. Am.* **81,** 1573–1602.

Wald, D. and T. Heaton (1994). Spatial and temporal distribution of slip for the 1992 Landers, California, earthquake, *Bull. Seism. Soc. Am.* **84,** 668–691.

Wald, D., D. Helmberger, and T. Heaton (1991). Rupture model of the 1989 Loma Prieta earthquake from the inversion of strong motion and broadband teleseismic data, *Bull. Seism. Soc. Am.* **81,** 1540–1572.

Wells, D. and K. Coppersmith (1994). New empirical relationships among magnitude, rupture length, rupture width, rupture area, and surface displacement, *Bull. Seism. Soc. Am.* **84,** 974–1002.

Department of Earth Sciences
Carleton University
1125 Colonel By Dr.
Ottawa, Ontario, Canada K1S 5B6
gma@ccs.carleton.ca
(G.M.A)

Pacific Engineering and Analysis
311 Pomona Ave.
El Cerrito, California 94530
(W.S.)

Manuscript received 8 May 1996.

Appendix

Regression Results for California Earthquakes

		Frequency:		0.20	0.28	0.40	0.56	0.79	1.1	1.6	2.2	3.2	4.5	6.3	8.9	12.6
Attenuation $c(f)$				0.0001	0.0002	0.0006	0.0005	0.0021	0.0021	0.0024	0.0021	0.0030	0.0040	0.0047	0.0053	0.0061
added depth $h(f)$				8	4	4	5	7	7	10	12	14	15	14	12	14
log s_j(soil C/D)				0.14	0.19	0.18	0.18	0.15	0.15	0.16	0.13	0.08	0.02	−0.03	−0.06	−0.10
Source Terms:																
Date		**M**	**m**					log $A(CM/S)$ at R = 1 km								
1952	0721	7.4	7.2		2.68	2.79	2.84	3.15	3.24	3.12	3.09	3.10	3.03	2.83	2.59	
1966	0628	6.1	6.1		1.89	2.08	2.09	2.31	2.32	2.40	2.65	2.61	2.47	2.42	2.16	2.09
1968	0409	6.8	6.4	2.03	2.29	2.53	2.46	2.66	2.65	2.69	2.60	2.67	2.72	2.55	2.34	
1970	0912	5.4	5.6				1.58	1.80	2.02	2.11	2.25	2.36	2.44	2.39	2.23	2.00
1971	0209	6.6	6.3	1.93	2.00	2.12	2.19	2.45	2.54	2.59	2.61	2.73	2.72	2.64	2.47	2.28
1974	1128	5.2	5.5				1.89	1.86	1.85	2.12	2.34	2.40	2.29	2.22	2.15	2.04
1975	0808	4.7	4.9					1.53	1.67	1.51	1.62	1.81	1.92	2.06	1.94	2.02
1975	0802	4.4	4.7				1.60	1.51	1.54	1.70	1.78	2.05	2.01	1.85	1.84	1.70
1975	0607	5.2	6.3				1.54	2.21	2.30	2.41	2.53	2.59	2.74	2.66	2.46	2.35
1979	0806	5.7	6.0	1.89	1.61	1.77	1.94	2.18	2.37	2.45	2.53	2.54	2.48	2.30	2.06	1.84
1979	1015	6.5	6.5	2.53	2.42	2.51	2.53	2.61	2.62	2.73	2.76	2.80	2.76	2.67	2.49	2.31
1979	1015	5.2	5.6				1.98	2.09	2.20	2.33	2.42	2.44	2.37	2.26	2.14	1.98
1980	0527	6.0	6.6		2.18	2.47	2.43	2.61	2.89	2.90	2.88	2.80	2.95	2.90	2.80	2.70
1980	0525	5.7	6.0			1.41	1.68	2.13	2.26	2.56	2.50	2.65	2.45	2.55	2.27	2.19
1980	0527	4.9	5.2			0.97	1.07	1.60	1.85	1.98	2.12	2.18	2.10	1.90	1.68	1.62
1980	0611	5.0	4.7					1.17	1.30	1.38	1.48	1.65	1.84	1.84	1.84	1.88
1980	0531	4.9	5.3			1.03	1.26	1.48	1.76	1.99	2.18	2.26	2.41	2.25	2.09	1.95
1980	0525	6.0	6.2	1.77	2.02	2.32	2.17	2.48	2.30	2.55	2.65	2.74	2.67	2.50	2.30	2.12
1980	0127	5.4	5.7		1.69	1.56	1.78	2.09	2.34	2.44	2.40	2.49	2.34	2.21	1.76	1.44
1980	0124	5.8	5.9	1.92	1.97	2.17	2.37	2.41	2.45	2.45	2.52	2.54	2.46	2.19	1.79	1.32
1980	0225	4.9	5.2				1.41	1.53	1.84	2.08	2.13	2.15	2.20	2.13	1.92	1.96
1980	0525	5.7	6.2					2.36	2.43	2.63	2.66	2.74	2.68	2.68	2.47	2.37
1980	0525	6.3	6.6	2.01	2.17	2.19	2.38	2.41	2.41	2.75	2.87	2.84	2.92	2.81	2.72	2.61
1981	0426	5.8	6.3	2.11	2.02	2.19	2.33	2.42	2.50	2.62	2.65	2.68	2.79	2.65	2.49	2.36
1983	0611	5.3	5.4	1.79	1.51	1.56	1.91	2.06	1.99	2.08	2.08	2.30	2.25	2.05	1.76	1.37
1983	0509	5.0	5.6	1.04	1.24	1.38	1.53	1.80	1.91	2.14	2.29	2.45	2.46	2.28	2.05	1.83
1983	0709	5.2	5.8		1.51	1.46	1.66	1.76	1.98	2.24	2.45	2.57	2.54	2.57	2.27	2.07
1983	0722	5.8	6.3	2.15	2.20	2.12	2.17	2.47	2.55	2.71	2.75	2.80	2.78	2.69	2.49	2.28
1983	0502	6.4	6.7	2.25	2.40	2.58	2.70	3.01	2.91	2.99	2.95	2.85	2.72	2.48	2.18	1.84
1984	0424	6.2	6.3	1.81	1.85	2.00	2.12	2.55	2.52	2.59	2.65	2.68	2.66	2.46	2.16	1.86
1986	0126	5.4	5.8	1.40	1.81	2.08	2.10	2.41	2.29	2.41	2.42	2.46	2.45	2.30	2.11	1.95
1986	0721	6.2	6.4	2.12	2.11	2.27	2.48	2.57	2.47	2.65	2.74	2.75	2.73	2.57	2.39	2.23
1986	0721	5.6	5.3		1.10	1.42	1.69	1.94	1.85	2.15	2.10	2.12	2.30	2.11	2.14	1.97
1986	0708	6.0	6.3	1.96	1.92	2.06	2.21	2.38	2.51	2.58	2.58	2.69	2.75	2.73	2.65	2.49
1986	0720	5.9	5.8	1.76	1.68	1.73	1.86	2.15	2.23	2.38	2.45	2.38	2.43	2.39	2.22	1.95
1986	0731	5.8	5.9	1.46	1.72	1.81	1.96	2.07	2.29	2.38	2.53	2.48	2.41	2.34	2.32	2.03
1987	1001	6.0	6.3	1.77	1.92	1.93	2.05	2.27	2.47	2.63	2.67	2.74	2.77	2.70	2.55	2.36
1987	1124	6.7	6.7	2.49	2.41	2.80	2.78	2.86	2.84	2.84	2.84	2.88	2.82	2.80	2.68	2.44
1987	1004	5.3	5.8			1.82	1.99	2.16	2.30	2.42	2.45	2.62	2.51	2.46	2.32	2.13
1989	1018	6.9	7.2	2.60	2.70	2.72	2.86	3.08	3.09	3.10	3.05	3.02	2.91	2.78	2.53	2.24
1992	0628	7.3	7.2	2.77	2.70	2.91	2.94	3.12	3.10	3.07	3.03	3.07	3.10	3.00	2.80	2.57
1992	0425	7.1	7.0	2.69	2.71	2.88	2.85	2.90	2.85	2.96	2.97	3.02	3.05	2.95	2.64	2.40
1994	0117	6.7	7.0	2.42	2.39	2.54	2.66	2.87	2.96	3.05	3.07	3.09	3.04	2.91	2.69	2.43
Crust $V(f)$																
(implicit)				1.30	1.38	1.43	1.50	1.56	1.62	1.73	1.90	2.19	2.24	2.30	2.32	2.34
Quadratic Source Coef.																
		x0		1.92	1.96	2.10	2.18	2.41	2.46	2.60	2.65	2.68	2.66	2.56	2.35	2.14
		x1		0.628	0.621	0.730	0.587	0.599	0.534	0.473	0.415	0.366	0.347	0.326	0.296	0.268
		x2		−0.017	−0.032	−0.113	−0.003	−0.060	−0.048	−0.108	−0.114	−0.067	−0.053	−0.058	−0.044	+0.015